

## Attributing Observed SST Trends and Subcontinental Land Warming to Anthropogenic Forcing during 1979–2005

DUO CHAN AND QIGANG WU

*School of Atmospheric Sciences, Nanjing University, Nanjing, China*

(Manuscript received 2 April 2014, in final form 4 January 2015)

### ABSTRACT

Attribution studies conclude that it is extremely likely that most observed global- and continental-scale surface air temperature (SAT) warming since 1950 was caused by anthropogenic forcing, but some difficulties and uncertainties remain in attribution of warming in subcontinental regions and at time scales less than 50 years. This study uses global observations and CMIP5 simulations with various forcings, covering 1979–2005, and control runs to develop confidence intervals, to attribute regional trends of SAT and sea surface temperature (SST) to natural and anthropogenic causes.

Observations show warming, significantly different from natural variations at the 95% confidence level, over one-third of all grid boxes, and averaged over 15 of 21 subcontinental regions and 6 of 10 ocean basins. Coupled simulations forced with all forcing factors, or greenhouse gases only, reproduce observed SST and SAT patterns. Uncoupled AMIP-like atmosphere-only (prescribed SST and atmospheric radiative forcing) simulations reproduce observed SAT patterns. All of these simulations produce consistent net downward longwave radiation patterns. Simulations with natural-only forcing simulate weak warming. Anthropogenic forcing effects are clearly detectable at the 5% significance level at global, hemispheric, and tropical scales and in nine ocean basins and 15 of 21 subcontinental land regions. Attribution results indicate that ocean warming during 1979–2005 for the globe and individual basins is well represented in the CMIP5 multimodel ensemble mean historical simulations. While land warming may occur as an indirect response to oceanic warming, increasing greenhouse gas concentrations tend to be the ultimate source of land warming in most subcontinental regions during 1979–2005.

### 1. Introduction

Attribution studies have indicated that it is extremely likely that there has been a substantial anthropogenic contribution to global and continental surface air temperature (SAT) increases since the middle of the twentieth century (Hegerl et al. 2007; Bindoff et al. 2014). On subcontinental and smaller scales, the relative contribution of internal variability compared to the forced response to observed changes tends to be larger, since spatial differences in internal variations are averaged out in large-scale means. Several recent studies have applied attribution analyses to subcontinental scale regions since 1950 (Zhang et al. 2006; Min and Hense 2006; Jones et al. 2008; Wu 2010; Christidis et al. 2010, 2012;

Knutson et al. 2013; Jones et al. 2013). These studies concluded that it is likely that anthropogenic forcing has made a substantial contribution to warming of the inhabited continents over 50-yr or longer periods.

Several traditional Atmospheric Model Intercomparison Project (AMIP) experiments, forced by prescribed observed sea surface temperature (SST) and sea ice, successfully capture patterns of observed trends in SAT (Compo and Sardeshmukh 2009; Dommenget 2009; Pégion and Kumar 2010; Shin and Sardeshmukh 2011) and atmospheric circulation (Deser and Phillips 2009) in the period of 1950–2000. These studies find that most land warming is caused by ocean warming and not by the local response to radiative forcings, thus emphasizing the significant role of remote oceanic influences on continental warming. We compare the 20-yr observed SAT trend over the period of 1980–99 with corresponding forced trends from phase 3 of the Coupled Model Intercomparison Project (CMIP3) AMIP and twentieth-century historical simulation (20C3M) experiments, and

Corresponding author address: Prof. Qigang Wu, School of Atmospheric Sciences, Nanjing University, Hankou Road #22, Nanjing, Jiangsu 210093, China.  
E-mail: qigangwu@nju.edu.cn

find that both CMIP3 20C3M and AMIP multimodel ensemble mean simulations reproduce observed SAT trend patterns, and these two simulations produce consistent net downward longwave radiation (RLDS) and SAT trend patterns (see the appendix). [Compo and Sardeshmukh \(2009\)](#) suggest that the recent oceanic warming has caused the continents to warm through a hydrodynamic–radiative teleconnection mechanism: 1) the warmed ocean tends to release more water vapor and increase the specific humidity at every level of the atmosphere, which will in turn increase downwelling longwave radiation and surface temperature; and 2) increased SST further influences land warming by adjusting atmospheric circulation, leading to changes in cloud cover and absorption of downwelling shortwave radiation in some land regions. Many aspects of the response of SAT to global SST changes can be reproduced in simulations in which SST changes are prescribed only in the tropics (e.g., [Hoerling et al. 2001](#); [Schneider et al. 2003](#); [Hurrell et al. 2004](#); [Deser and Phillips 2009](#); [Shin and Sardeshmukh 2011](#)).

The oceans may themselves have warmed (or cooled in small areas) from a combination of natural variability and anthropogenic influences. The last two Intergovernmental Panel on Climate Change (IPCC) reports conclude that the warming of the upper several hundred meters of ocean during the second half of the twentieth century was “likely” to have been caused by anthropogenic forcing ([Hegerl et al. 2007](#); [Bindoff et al. 2014](#)). Recent studies find that upper-ocean temperature changes during the second half of the twentieth century are consistent with the changes expected due to human forcing of the climate system ([Barnett et al. 2005](#); [Gleckler et al. 2012](#); [Pierce et al. 2012](#)). But [Shin and Sardeshmukh \(2011\)](#) show that several fully coupled GCMs, forced by prescribed observational radiative forcings, tend to largely underestimate the magnitude of the observed tropical SST trend during 1950–2000 over the Indian Ocean and east Pacific, and generally do not capture the regional trend pattern of SAT over landmasses surrounding the North Atlantic Ocean.

The land and ocean warming trend has intensified since the late 1970s ([Trenberth et al. 2007](#)), resulting in significant regional ecosystem and societal impacts ([Rosenzweig et al. 2008](#)). An estimate of the anthropogenic contribution to recent temperature trends at subcontinental scales is of considerable practical importance, as natural and human systems are more likely to be affected by regional temperature changes when these changes are outside the range normally experienced. Although [Knutson et al. \(2013\)](#) have found anthropogenic-induced land warming trends in several continental and large land regions since the 1970s, we intend to investigate what proportion of land warming in 21 subcontinental regions

TABLE 1. Abbreviated names and coordinates for oceanic regions, and the subcontinental regions (from [Giorgi 2002](#)) used in the analysis.

Region name and abbreviation	Coordinates	
	Longitude	Latitude
Northern Hemisphere	NH	0°–360° 0°–90°N
Southern Hemisphere	SH	0°–360° 0°–90°S
Tropical Ocean	TO	0°–360° 20°S–20°N
Tropical Indian Ocean	TIO	40°–120°E 20°S–20°N
Tropical west Pacific	TWP	110°–155°E 20°S–20°N
Tropical Atlantic Ocean	TAO	70°W–10°E 20°S–20°N
North Pacific Ocean	NPO	120°E–120°W 20°–70°N
South Pacific Ocean	SPO	140°E–70°W 60°–20°S
North Atlantic Ocean	NAO	90°W–0° 20°–70°N
Tropical central Pacific	TCP	170°–125°W 20°S–20°N
Tropical eastern Pacific	TEP	125°–75°W 20°S–20°N
South Indian Ocean	SIO	15°–140°E 60°–20°S
South Atlantic Ocean	SAO	65°W–15°E 60°–20°S
Northern South America	NSA	80°–35°W 20°S–10°N
Mexico	MEX	115°–80°W 10°–30°N
Western North America	WNA	130°–105°W 30°–60°N
Greenland	GRL	105°–10°W 50°–80°N
Mediterranean	MED	10°W–40°E 30°–50°N
Northern Europe	NEU	10°W–40°E 50°–75°N
Western Africa	WAF	20°W–20°E 10°S–20°N
Eastern Africa	EAF	20°–50°E 10°S–20°N
Southern Africa	SAF	10°–40°E 35°–10°S
Northern Africa	NAF	20°W–65°E 20°–30°N
East Asia	EAS	100°–145°E 20°–50°N
Central Asia	CAS	40°–75°E 30°–50°N
Tibetan	TIB	75°–100°E 30°–50°N
Siberian	SIB	40°E–180° 50°–70°N
Central North America	CNA	105°–85°W 30°–50°N
Alaska	ALA	170°–105°W 60°–70°N
Southeast Asia	SEA	90°–155°E 10°S–20°N
South Asia	SAS	65°–100°E 5°–30°N
Eastern North America	ENA	85°–60°W 20°–50°N
Australia	AUS	110°–155°E 40°–10°S
Southern South America	SSA	75°–40°W 60°–20°S

can be attributed to external anthropogenic forcing or global ocean warming, and further quantify contributions of anthropogenic and natural forcings to observed subcontinental warming trends through an attribution study. Considering the importance of the correct representation of SST changes for simulating land warming ([Shin and Sardeshmukh 2011](#)), we will also examine whether the global and tropical ocean warming is well reproduced since 1979 in phase 5 of the Coupled Model Intercomparison Project (CMIP5; [Taylor et al. 2012](#)) runs through the attribution study and the global field significance test.

CMIP5 updates the previous CMIP3 experiment and contains a large multimodel archive of forced simulations. We use CMIP5 model run outputs to investigate what proportion of observed ocean warming during 1979–2005 can be attributed to external anthropogenic forcing, and then clarify the relative importance of

TABLE 2. CMIP5 model runs downloaded for this study from <http://cmip-pcmdi.llnl.gov/cmip5/index.html>. The top headings identify data types, grids of monthly average surface air temperature (SAT), net downward longwave radiation (RLDS), and sea surface temperature (SST). Subheadings CTR indicate the length (yr) of the preindustrial control simulation for each model, and the number of initial condition ensemble members for historical atmospheric-only runs with prescribed SST and atmospheric radiative forcing (AMIP), historical runs with all anthropogenic and natural forcings (HIST), historical runs with greenhouse gas forcing (GHG), and historical runs with natural forcing (NAT). All historical runs cover 1979–2005. The bottom row (SUM) shows total years of CTR simulations and all other columns show the number of ensemble members. (Expansions of all model names are available online at <http://www.ametsoc.org/PubsAcronymList>.)

Models	SAT/RLDS					SST			
	CTR	AMIP	HIST	GHG	NAT	CTR	HIST	GHG	NAT
ACCESS1.0		1	1				1		
BCC-CSM1.1		3	3	1	1		3	1	1
BCC-CSM1.1(m)		3	3			400	3		
CanESM2	995		5	5	5		5	5	5
CCSM4	500	5	6	3	4	500	6	3	3
CESM1-CAM5		2	3			320	3		
CMCC-CESM			1				1		
CMCC-CM		3	1				1		
CNRM-CM5	800	1	5	5	5		5	5	5
CSIRO-Mk3.6.0	500	9	9	5	5		9	5	5
FGOALS-g2	700	1	5	1	3		5		
GFDL-CM3	500	5	5	3	3	500	5	3	3
GFDL-ESM2G	500		1			500	1		
GFDL-ESM2M	500		1	1	1	500	1	1	1
GFDL-HIRAM-C180		3							
GISS-E2-H	540		5	5	5		5	3	5
GISS-E2-R	550	6	5	5	5	550	6	5	5
HadGEM2-A		1							
HadGEM2-AO			1				1		
HadGEM2-CC	242		1			242	1		
HadGEM2-ES	337	—	4	4	4	496	4	4	4
INM-CM4		1	1				1		
IPSL-CM5A-LR	1000	5	5	3	3	1000	5	3	3
IPSL-CM5A-MR	300	3	3	3		300	3	3	2
IPSL-CM5B-LR	300	1	1			300	1		
MIROC-ESM	530		3	3	3	680	3		
MIROC-ESM-CHEM	255		1	1	1				
MIROC5	600	2	1			600	1		
MPI-ESM-LR	1000	3	3			1000	3		
MPI-ESM-MR	1000	3	3				3		
MRI-CGCM3	500	3	3	1	1	500	3	1	1
MRI-ESM1			1				1		
NorESM1-M	500	3	3	1	1	500	3	1	1
SUM	12649	67	93	50	50	8888	89	43	44

external radiative forcing changes (due to greenhouse gases and other factors) and global SST warming on subcontinental SAT trends. The trend over 1950–78 is nearly zero in the global mean temperature, and 1979 approximately reflects the beginning of the peak warming period. The 1979–2005 period is chosen since most CMIP5 historical runs end in 2005 (projected forcing is used starting 2006) and AMIP-like runs in CMIP5 are from 1979 to 2008. Our study is complementary to previous attribution studies that focus on SAT and SST trends over 50-yr and longer periods and thereby strengthens existing detection and attribution evidence.

The paper is arranged as follows. Section 2 describes the data sources and analysis techniques. Section 3 investigates attribution of SAT and SST trends on global, hemispheric, and regional land or ocean basin scales. Section 4 summarizes conclusions.

## 2. Data and method

Observed data are obtained from HadCRUT4 (Kennedy et al. 2011), a blend of the CRUTEM4 land SAT and HadSST3 SST datasets, for 1979–2005 on a 5° latitude–longitude grid. Only grid boxes having more than 66% of years available are included in the trend

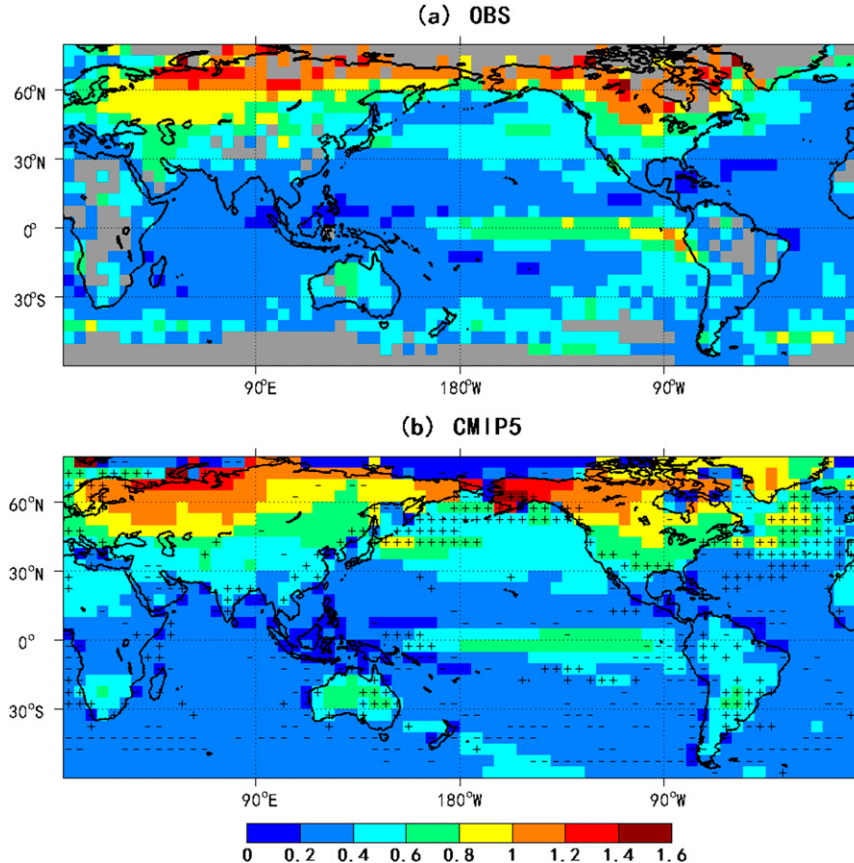


FIG. 1. The standard deviations of annual mean SAT and SST in (a) observations and (b) the CMIP5 multimodel control simulations. Plus/minus symbols mark individual grid boxes with ratio of simulated and observed variance exceeding the 5% significance level in the F test.

analysis. We consider trends of surface temperature for the globe, NH and SH ocean and land, the tropics, 10 ocean basins, 6 continental and 21 large subcontinental land regions (see Table 1 and Fig. 2f; abbreviations for regions are expanded in Table 1), and individual grid boxes. The 21 subcontinental regions are defined by Giorgi (2002); they represent different climatic regimes while approximately covering all land areas except Antarctica. Since Australia has an area similar to the other subcontinental areas, it is counted as either a continental or subcontinental region depending on the analysis.

The natural variability of linear trends in surface temperature (both SAT and SST) is calculated from the preindustrial control runs which were produced by CMIP5 (Taylor et al. 2012). A total of about 12 000 (8800) years of preindustrial control simulations from models in Table 2 are used to estimate the natural variability of trends in SAT (SST). The climate drift of control simulations at each grid box is removed separately for each model. The control run and other forced

simulation data from the model grids are at a higher horizontal resolution than the observed datasets and have been averaged onto the observed 5° grid for the analysis. We have about 800 (500) realizations of estimated linear trends of SAT (SST) for the 27-yr period. The SAT and SST trends from the control runs are approximately normally distributed and the standard deviation ( $\sigma$ ) of this distribution is used as the measure of the natural variability of linear trends. In each region or grid box, we apply a one-sided local significance test to determine whether the observed SAT or SST trend (OBS) is significantly different from zero at the 5% significance level ( $|OBS| \geq +1.96\sigma$ ).

The range of fractions of grid boxes with significant trends that could occur due to internal variability is determined by applying the field significance test of Livezey and Chen (1983). On average, in a stationary climate, only 5% of the grid boxes are expected to show warming trends significant at the 95% confidence level due to random variability alone. As there is large spatial coherence of low-frequency variations of SST (also

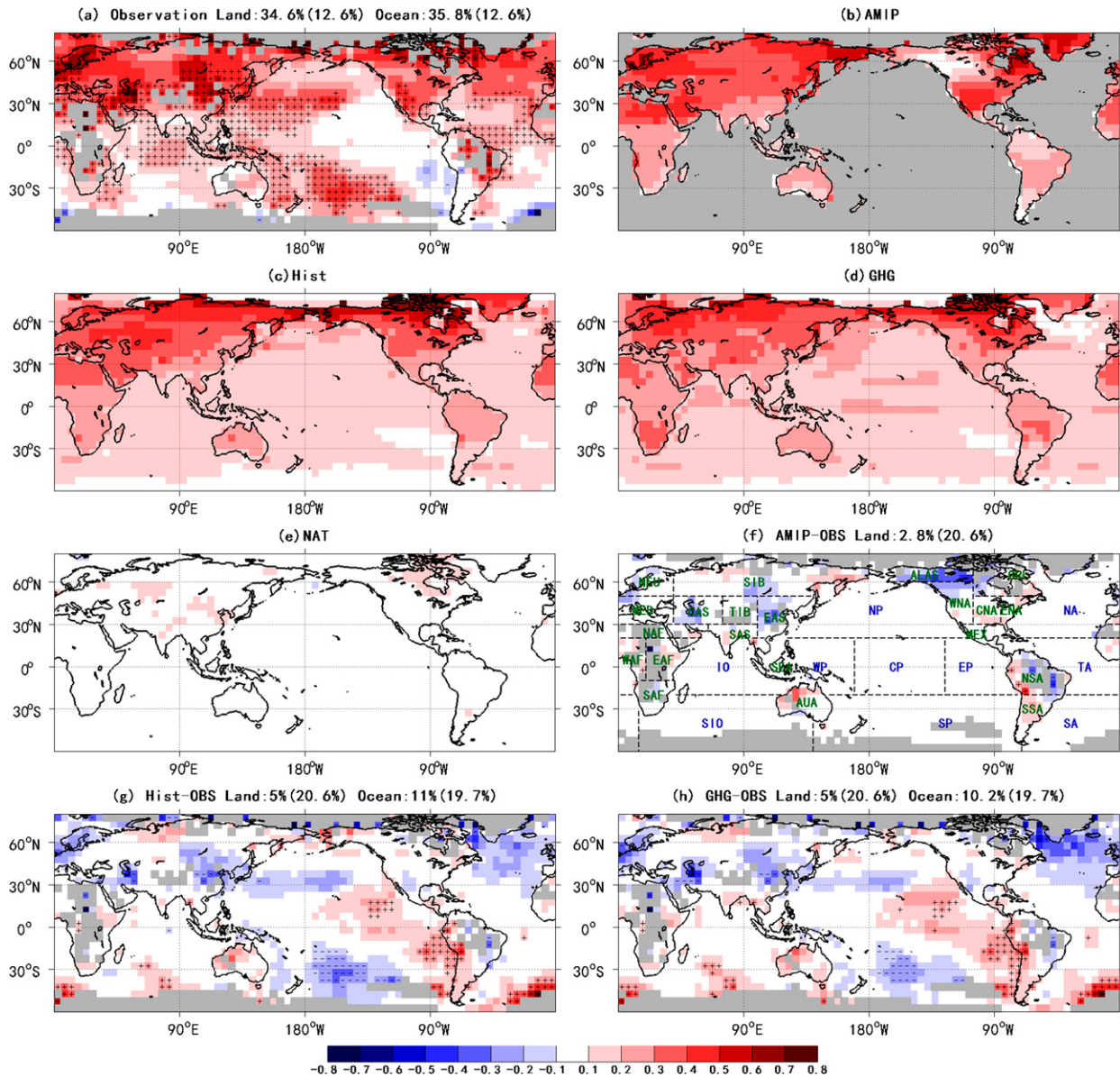


FIG. 2. Trends in annual mean surface temperature ( $^{\circ}\text{C decade}^{-1}$ ) during 1979–2005, including (a) observed trends from HadCRUT4, (b) multimodel ensemble-mean trends in AMIP, (c) Historical, (d) HistoricalGHG, and (e) HistoricalNAT simulations, and difference of trends (f) between AMIP and observations, and between (g) Historical and (h) HistoricalGHG and observations. Regions used in the analysis are marked in (f). Plus (minus) symbols mark individual grid boxes with significant warming/cooling trends in (a), and significantly larger (smaller) forced trends than observations in (f)–(h). Above each map is the fraction of grid boxes over global land and ocean with significant warming trends [in (a)] or significantly different trends [in (f)–(h)] and, in parentheses, the possible range of fractions that could occur due to internal variability. In (b), SST is a model input so differences between models and observations are not evaluated over oceans.

SAT), a much larger fraction of significant warming trend might occur by chance. For 27-yr trends, we consider the linear trends at each grid box from the control simulation and determine the fraction of grid boxes that show locally significant trends. This is repeated 800 (500) times to determine the distribution of grid box fractions with significant land (ocean) change that could occur due to internal climate variations.

To determine the possible roles of external anthropogenic and natural radiative forcings, and boundary forcings in the observed 1979–2005 SAT and SST trends, the modeled trends of SAT or SST are calculated from the following CMIP5 simulations for 1979–2005, as listed in Table 2: 1) forced by observed atmospheric composition changes (reflecting both anthropogenic and natural sources, and termed Historical or HIST in Table 2),

TABLE 3. Results of field significance tests. The two right columns show the percent of grid boxes over global ocean or land locally significant at the stated confidence level (95% one-sided or 90% two-sided, below) based on the specified condition in the left columns. The number in parentheses is the result of a field significance test to determine the largest value of this fraction due to natural climate variability. It represents at least the 95% significance level for the field significance of the fraction of grid boxes. (a) Percent of grid boxes over the global ocean and land with observed linear warming trends locally significant at the 95% confidence level. (b) As in (a), but for the fraction of grid boxes where the observed trend is significantly different from the ensemble mean forced trend in Historical, HistoricalGHG, HistoricalNAT and AMIP simulations, using a two-sided test at the 90% confidence level. (c),(d) As in (b), but for the fraction of grid boxes where the forced trend of SAT and downward long wave radiations (RLDS) in AMIP simulation is significantly different from that in Historical and HistoricalGHG simulations. (e) Same as in (c), but for the fraction of grid boxes where the forced trends of SAT and RLDS in Historical simulation are significantly different from that in HistoricalGHG simulation. Note that in (b) and (c), no ocean test is performed for any comparison involving AMIP data.

		Ocean	Land
(a) Grid boxes with observed trend significantly different from natural variations		35.8% (12.6%)	34.6% (12.6%)
(b) Grid boxes with observed trend significantly different from trend from simulation forced by stated factors	HIST	11.0% (19.7%)	5.0% (20.6%)
	GHG	10.2% (19.7%)	5.0% (20.6%)
	NAT	30.9% (19.7%)	26.5% (20.6%)
	AMIP		2.8% (20.6%)
(c) Grid boxes with AMIP SAT trend significantly different from trend from coupled simulation	HIST		4.9% (20.6%)
	GHG		5.8% (20.6%)
(d) Grid boxes with AMIP RLDS trend significantly different from trend from coupled simulation	HIST	2.6% (19.5%)	0.5% (21.2%)
	GHG	3.5% (19.5%)	1.1% (21.2%)
(e) Grid boxes with SAT or RLDS trend significantly different between runs with HIST or GHG forcing	SAT	0.0% (19.7%)	0.0% (20.6%)
	RLDS	0.0% (19.5%)	0.0% (21.2%)

2) greenhouse gas forcing only (HistoricalGHG or GHG), 3) natural climatic forcing only including volcanic eruptions and changes in the solar output (HistoricalNAT or NAT), and 4) AMIP-like runs forced with atmospheric radiative forcing and using observed SST and sea ice instead of the coupled ocean model (AMIP column in Table 2).

In the original AMIP experiment (Gates et al. 1999), atmospheric model integrations were driven by observed time-varying SSTs and sea ice as the lower boundary condition, and did not take into account the direct effects of atmospheric radiative forcing upon SAT. According to Deser and Phillips (2009), the new AMIP approach in CMIP5 does not “double count” the atmospheric radiative forcing because only the direct effect is specified, whereas the indirect effect is included in the prescribed SST forcing. Compo and Sardeshmukh (2009) found that the recent warming over land has occurred as a response to oceanic warming through enhanced RLDS due to increased atmospheric moisture rather than as a direct response to increasing greenhouse gases.

The cumulative significance of these 27-yr linear trends of annual mean surface temperature and other atmospheric fields in each region and grid box is assessed using the same method as for the observations. We also conduct a two-side consistency test to determine whether the difference between the observed and any simulated trend is significantly different from zero at the 90% confidence level at each region and grid box  $\{| \text{difference} | \geq 1.64\sigma \sqrt{[1 + 1/(Ne)]}\}$ , where Ne is the

number of ensemble members of the model signal in the last row of Table 2), and a field significance test to obtain the 95th percentile of the distribution of fractions of grid boxes that give significantly different trends due to internal variability.

Finally, a linear regression model is constructed to compare the observed and simulated temperature changes in each spatial region by expressing the observation ( $Y$ ) as a sum of two scaled response signals ( $X$ ) plus residual internal variability ( $e$ ):

$$Y(t) = b_{\text{ant}} X_{\text{ant}}(t) + b_{\text{nat}} X_{\text{nat}}(t) + e(t), \quad (1)$$

where  $X = (X_{\text{ant}}, X_{\text{nat}})$  are estimated responses to external anthropogenic forcings and natural forcings, and scaling factors ( $b_{\text{ant}}, b_{\text{nat}}$ ) are best estimated signal strengths that adjust the amplitudes of those two signals (Mardia et al. 1979; Hegerl et al. 2007; Bindoff et al. 2014). The climate response to external anthropogenic forcings (termed HistoricalANTH, including well-mixed greenhouse gas forcing and other components of anthropogenic forcing, such as the effect of sulfate aerosols including their indirect effect on the cloud albedo, tropospheric and stratospheric ozone, and land use changes) is represented by the difference between the ensemble mean of Historical and HistoricalNAT experiments. Note that we assume the linearity of forced signals here. Detection of an anthropogenic signal is claimed at the 5% significance level if the 95% confidence interval of its signal strength ( $b$  value) does not

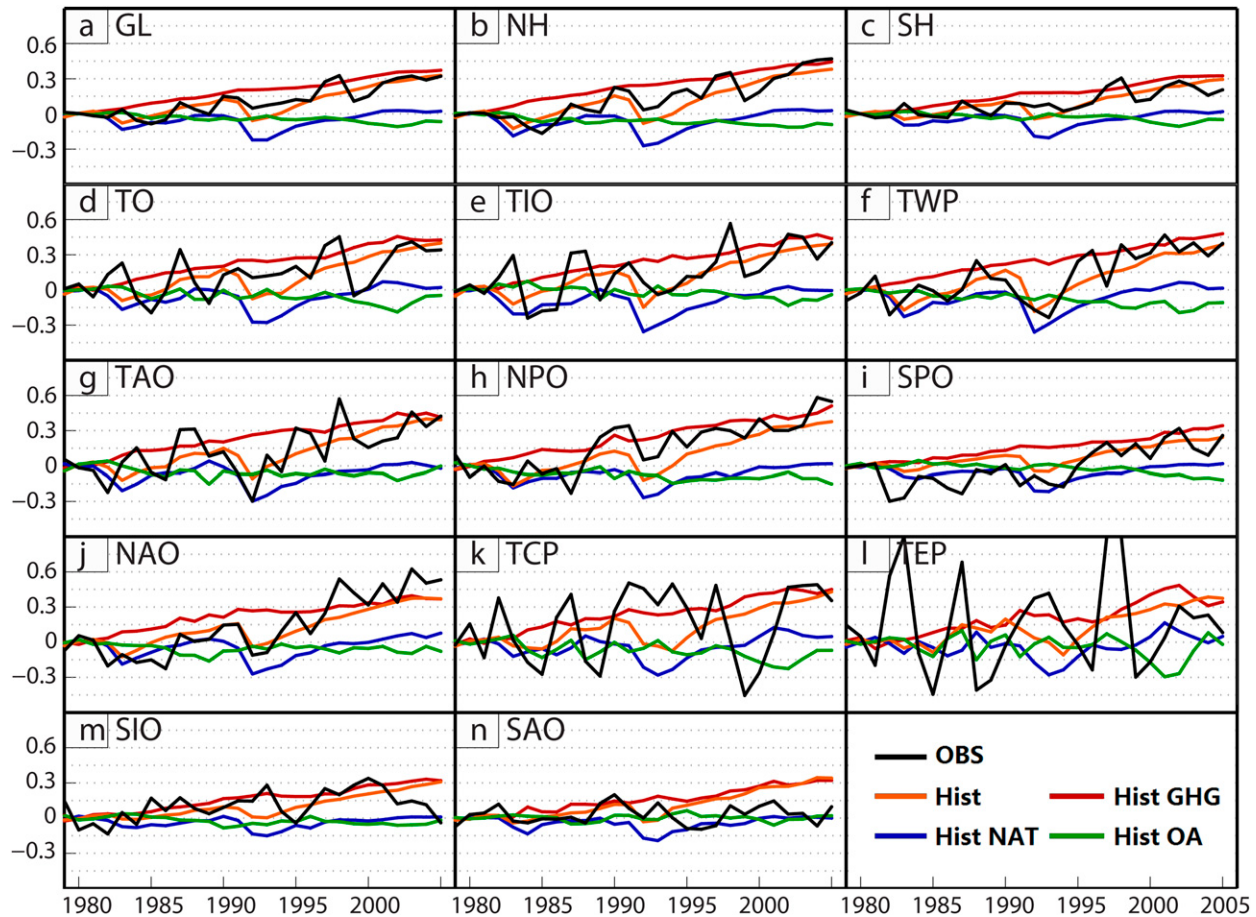


FIG. 3. Time series of annual mean observed (black lines) and ensemble-mean simulated SST anomalies averaged over the 14 ocean domains during 1979–2005. Simulated SST changes are from Historical (orange lines), HistoricalGHG (red lines), and HistoricalNAT (blue lines) experiments. SST changes from other anthropogenic forcing (HistoricalOANTH, green lines), represented by the difference of Historical minus the sum of HistoricalGHG and HistoricalNAT experiments, are plotted in green lines.

cross the zero line. An interval that includes  $b = 1$  suggests that the signal is consistent with the observed temperature change. The statistical significance of regression coefficients and correlation coefficients in the analyses is assessed using the  $t$  statistic. Because of autocorrelations in the SST or SAT fields, the effective sample sizes in the  $t$  tests are estimated using the relationship outlined in Davis (1976). The effective sample sizes range from 13 to 20 over ocean domains and from 12 to 21 over land regions.

### 3. Results

#### a. Comparison of observed and simulated variability

The observed variability of the detrended surface temperatures on interannual and longer time scales is compared with the variability in the control simulations to evaluate the quality of the simulations of natural internal climate variability. Simple linear detrending is used

to attempt to remove some of the possible anthropogenic signal in the observed temperatures. The results are insensitive to the order of the polynomial trend removed from the indices. The variances of the detrended observed and control simulated temperatures of each model are calculated at each of the grid boxes with sufficient observational data. An F test is utilized to determine whether the multimodel mean of simulated variance in control runs is significantly larger or smaller than the corresponding observed variance at each grid box at the 5% significance level.

Figure 1 shows the geographical distribution of observed (1979–2005, detrended) and CMIP5 model control run standard deviations of grid box annual averaged SAT (over land) and SST (over oceans). The general features of observed variability are well simulated through the multimodel ensemble-mean simulations. The spatial correlation coefficient between the observed and modeled standard deviation fields is 0.77, indicating

a good agreement between models and observations in the overall spatial structure of the variability.

In addition, the CMIP5 model has comparable or larger variability than observed over land, but substantially larger (smaller) variability than observed in the North Atlantic and Pacific (eastern tropical Indian Ocean and western tropical Pacific, eastern tropical Pacific, and high-latitude South Ocean). Knutson et al. (2013) also find that CMIP5 models simulate larger low-frequency internal variability than the observed estimate in high-latitude oceanic and continental regions of the Northern Hemisphere, but smaller internal variability over much of the remaining ocean regions and Southern Hemisphere. When averaged over each of the land and ocean regions in Table 1, the variability in the CMIP5 models is similar to or slightly larger than that observed (not shown). Therefore, the significance of detection and attribution results presented in this study is unlikely to be overestimated except over three ocean domains (SPO, SAO, and SIO).

*b. Detection of observational warming over land and ocean at various scales*

Figure 2a illustrates the spatial patterns of linear SAT trends for 1979–2005 in HadCRUT4, and contains similar features as in the IPCC Fourth Assessment Report (Trenberth et al. 2007, their Fig. 3.9). About one-third of the individual grid boxes (34.6% over land and 35.8% over ocean) with sufficient observational data show significant 27-yr warming trends at the 5% significance level, which is consistent with that in Knutson et al. (2013) but less than the fraction of significant 30-yr warming trend over the globe (about 45%) during 1973–2002 in Karoly and Wu (2005) and during 1971–2000 in Wu and Karoly (2007). Figure 2a shows more warming over land than ocean and especially at higher NH latitudes, but weak warming or cooling is seen in a few regions, especially the tropical eastern Pacific and midlatitudes of the SH oceans. These fractions of warming trends are much too large to be explained as a chance occurrence due to internal climate variations such as El Niño and the Pacific decadal oscillation (PDO; Mantua et al. 1997) (Fig. 2a and Table 3).

Observed SSTs over the globe, NH, SH, tropics, tropical Indian Ocean, tropical western Pacific and Atlantic, North and South Pacific, and North Atlantic have all increased in 1979–2005, showing significant warming trends at the 5% significance level (Figs. 3 and 4), but the other four basins (the tropical central and eastern Pacific and the South Indian and Atlantic Oceans) have weak warming with some areas of cooling. The globe, entire NH and SH, five continental regions, and 15 of 21 subcontinental regions show significant warming trends at

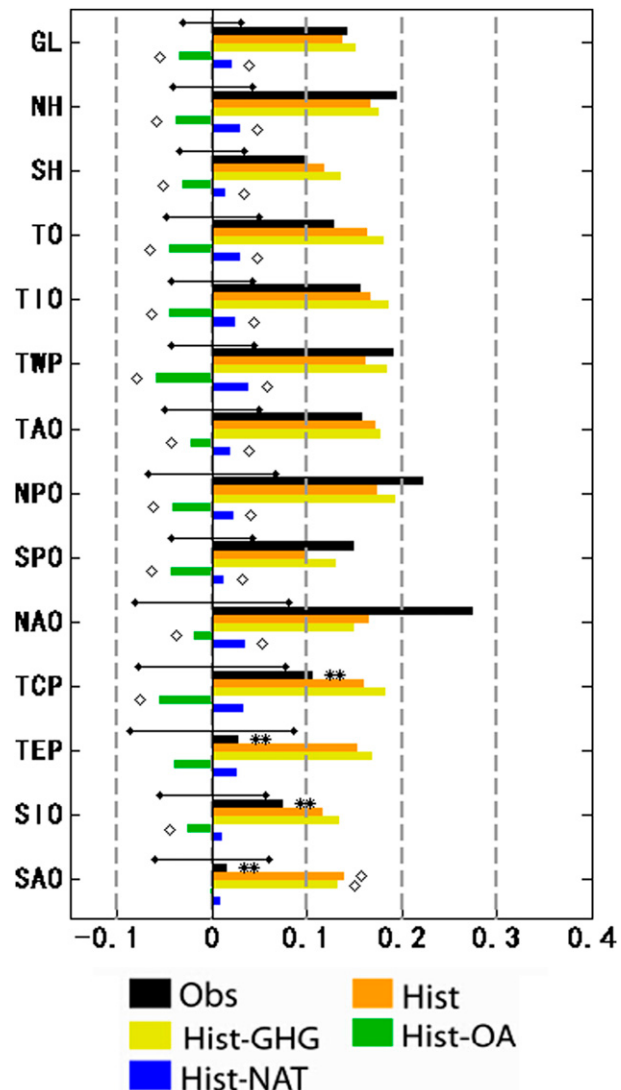


FIG. 4. Observed and simulated SST linear trends from 1979 to 2005 ( $^{\circ}\text{C decade}^{-1}$ ) averaged over 14 ocean domains. Each error bar at the left of an observed trend is the standard deviation ( $\sigma$ ) of 500 samples of 27-yr SST from 8000 years of CMIP5 control runs and represents the natural variability of the observed or modeled trend of SST averaged over the spatial domain. Observed trends significant at the 5% level are unmarked; significant and insignificant at the 10% level are marked with one and two stars, respectively. A forced trend significantly different from the corresponding observed trend at the 90% confidence level is marked with the diamond symbol.

the 5% significance level (Figs. 5 and 6), and three other regions (Alaska, South Asia, and central North America) show significant warming trends at the 10% significance level. A field significance test is performed for the 21 Giorgi regions and 10 ocean basins in Table 1. At the 5% significance level, only 1 of 21 Giorgi regions and 1 of 10 of ocean regions show significant warming trend patterns. Therefore, the fact that 15 of 21 subcontinental

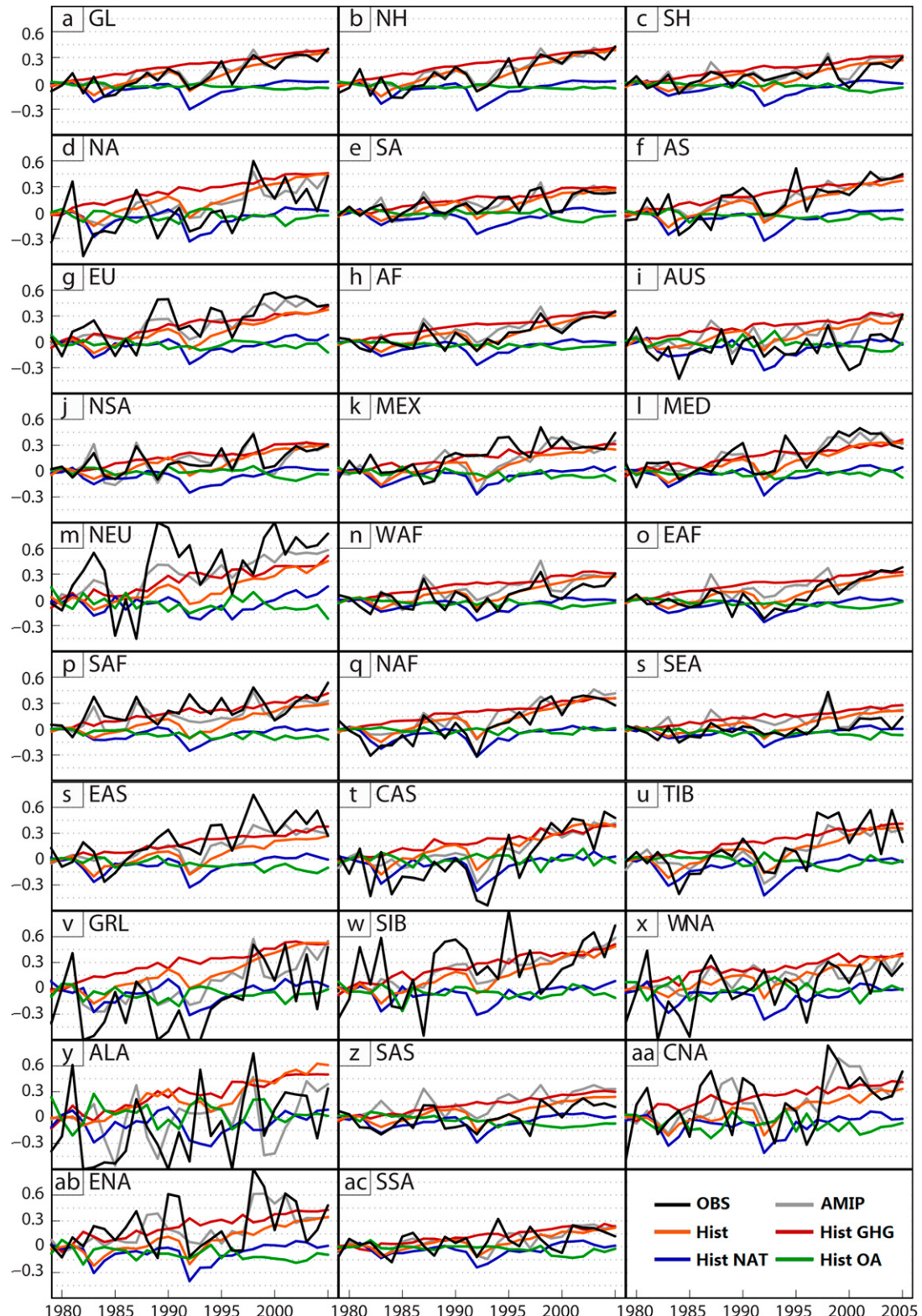


FIG. 5. As in Fig. 3, but for SAT time series in a range of land areas. Simulated SAT changes from the AMIP experiment are plotted in gray color.

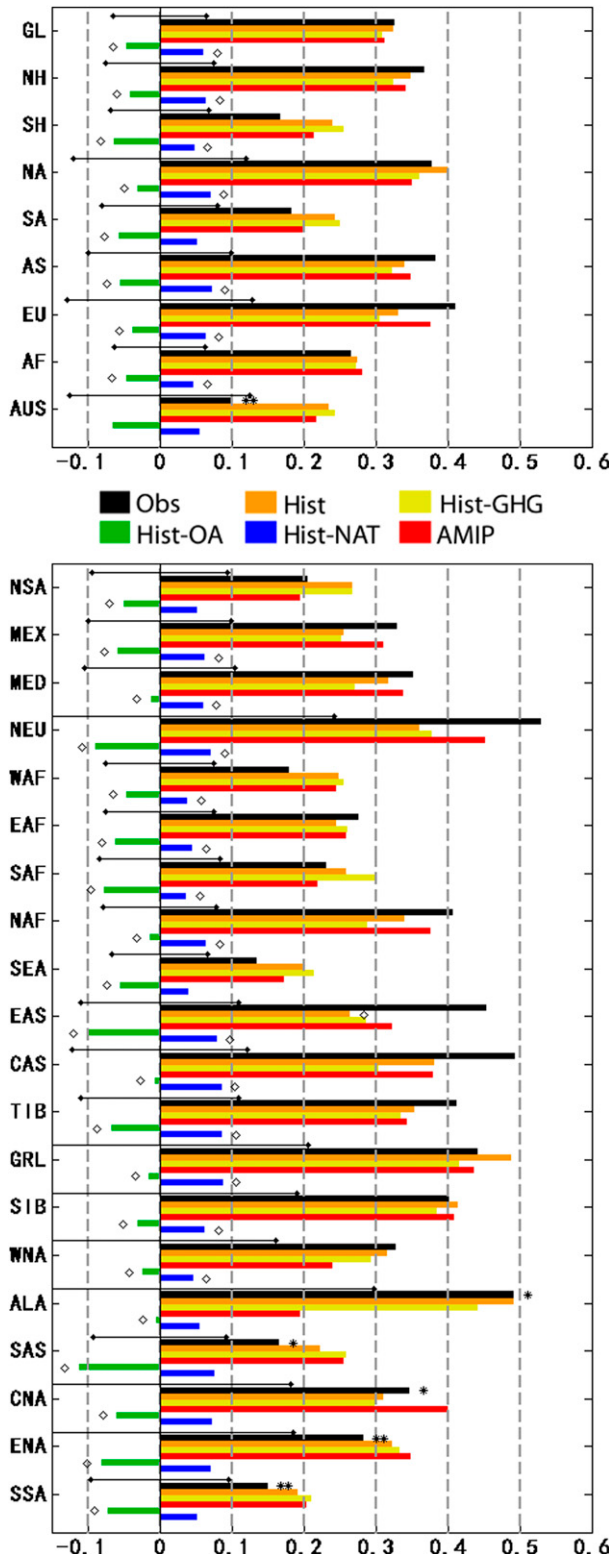


FIG. 6. As in Fig. 4, but for SAT linear trends (including AMIP trends, not evaluated over oceans in Fig. 4) over a range of land areas.

regions and 6 of 10 basin oceans show significant observed linear warming trends at the 5% significance level cannot be explained by internal variability.

### c. Attribution of SST trend

The multimodel ensemble mean is able to reproduce many features of the evolution of temperature change in most regions when models include anthropogenic and natural forcings. For example, the cooling of global, hemispheric, and basin-scale SST in HadSST3 is clearly seen after volcanic eruptions, particularly the eruption of Mt. Pinatubo in June 1991 (Fig. 3). Figure 3 also shows that there is a clear separation between the ensembles of simulations that include only natural forcings and those that contain anthropogenic forcing. For each domain, the GHG forcing captures most of the warming SST trend, and NAT forcing also contributes to a part of the warming SST trend, but other anthropogenic forcing results in a cooling SST trend (Figs. 3 and 4). A consistency test indicates that the simulated trends in Historical and HistoricalGHG are consistent with corresponding observed trends at each of the above 10 regions with significant observed trends, but not for the HistoricalNAT at the 10% significance level. Results using scaling factors in Fig. 7 demonstrate that a significant anthropogenic signal is robustly detectable in 12 domains and consistent with observed SST changes in 11 of 12 domains. Meanwhile, a significant NAT signal is also detectable in seven domains (GL, NH, TIO, TWP, TAO, SPO, and NAO), indicating that natural external forcing including volcanic eruptions and changes in the solar output slightly contributes to SST warming trends in these seven domains. The linear trend in natural forcing appears positive over the period 1979–2005 (Fig. 8.19 in Myhre et al. 2013). Overall, the above results suggest that increases in well-mixed greenhouse gases are the main driver of significant increases of SST at global, hemispheric, and tropical scales, and in six basins (TIO, TWP, TAO, NPO, SPO, and NAO) in the period of 1979–2005.

Further evidence is provided by the comparison between spatial patterns of observed (HadSST3) and simulated SST changes. The SST trends in both Historical and HistoricalGHG simulations (Figs. 2c,d) show a pattern of spatially near-uniform warming similar to that observed, especially over the tropical Indian Ocean, tropical west Pacific, and tropical Atlantic. Difference patterns resemble a PDO-like structure (Mantua et al. 1997) or interdecadal Pacific oscillation (IPO)-like structure (Power et al. 1999) in the Pacific (cooling in the North Pacific and South Pacific and warming in the eastern tropical Pacific) and negative AMO-like pattern in the North Atlantic (Enfield et al. 2001) (Figs. 2g,h).

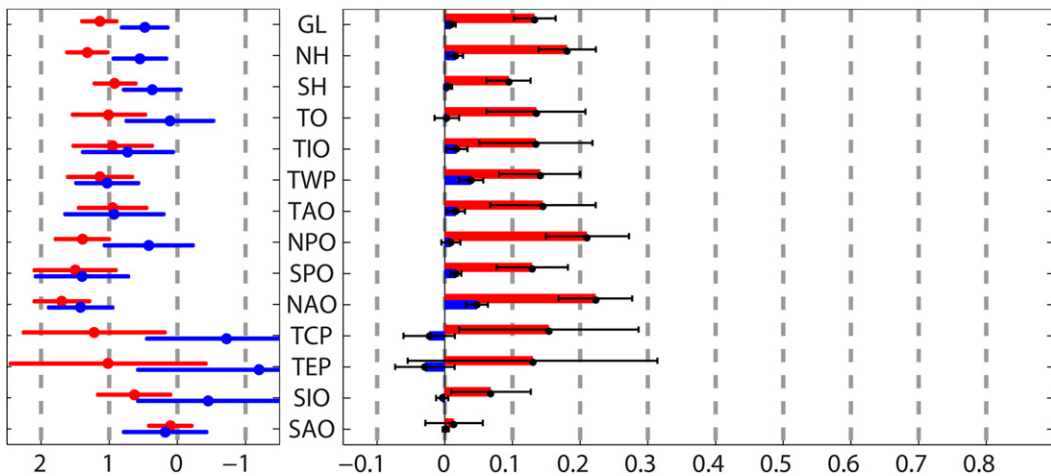


FIG. 7. (left) Estimated scaling factors indicating the match between observed and simulated SST trends when the external anthropogenic forcing (ANTH) and natural forcing (NAT) signals are taken into account in the linear regression model, and (right) estimated contributions of ANTH and NAT forcing components to observed temperature trends ( $^{\circ}\text{C decade}^{-1}$ ) over each domain, with their 2.5%–97.5% confidence intervals indicated for all 14 ocean domains. Red (blue) is for the ANTH (NAT) signal.

Larger decadal and multidecadal variations are seen in the observations than in the ensemble mean model simulations because the ensemble averaging process filters out much of the natural internal variability simulated by individual models. Despite the lack of detectable trends over many grid boxes, the observed trends are at least consistent with the historical runs in the North Atlantic, which have a very wide 5th to 95th percentile range of trends due to the large simulated internal variability. However, only about 11% of grid boxes over ocean where the observed trends are not consistent with the multimodel averaged trends at the 10% significance level for both Historical and HistoricalGHG simulations can be explained by internal climate variations (Table 3). About 31% of ocean grid boxes show significantly different observed and forced trends in the HistoricalNAT simulation, indicating that observed changes are much too large to be explained as a chance occurrence due to internal climate variations or external natural forcing.

Together with globally averaged SST results in Figs. 3 and 4, the global field consistency test in Figs. 2g and 2h strongly supports a human-induced warming of the world's ocean during 1979–2005. Gleckler et al. (2012) and Pierce et al. (2012) find an anthropogenic increase in global ocean heat content in the latter half of the twentieth century, and we here provide compelling evidence of human influence at the global and tropical basin scales of the near-surface ocean warming observed since 1979.

Most CMIP5 historical runs are started nominally in 1850. All models use the same greenhouse gas forcing,

but may handle other forcings differently, and (except for AMIP runs) each model generates different ocean states starting with its control run, so ENSO and other variations occur in different years in each model except for AMIP runs. Although 1979 reflects the beginning of the peak warming period, observed hemispheric averaged SST warming accelerated around the middle 1970s and 1960s in the Northern Hemisphere and Southern Hemisphere respectively (see Fig. 3.4 in Trenberth et al. 2007), and many model historical runs also show accelerated warming before 1979 (not shown). To ensure that the relatively short 1979–2005 analysis period does not give artificial results, we repeat analyses of trends depicted in Figs. 2 and 4 using observed and forced SST trends for 1975–2005, 1970–2005, and 1965–2005 (not shown), and find little difference in results compared to 1979–2005. All results support an anthropogenic-induced warming of the world's ocean.

To improve the sample size, all ensembles of each model are used in the above calculations. However, the ensemble mean would smooth out interannual variability. As discussed above, peak warming periods differ in different ensemble members. We recalculate forced SST trends using only one member of each model and find that the main results do not change noticeably.

#### d. Attribution of land warming

Figure 2 demonstrates that AMIP, Historical, and HistoricalGHG simulations are realistic in capturing the observed overall land warming. The fraction of the grid

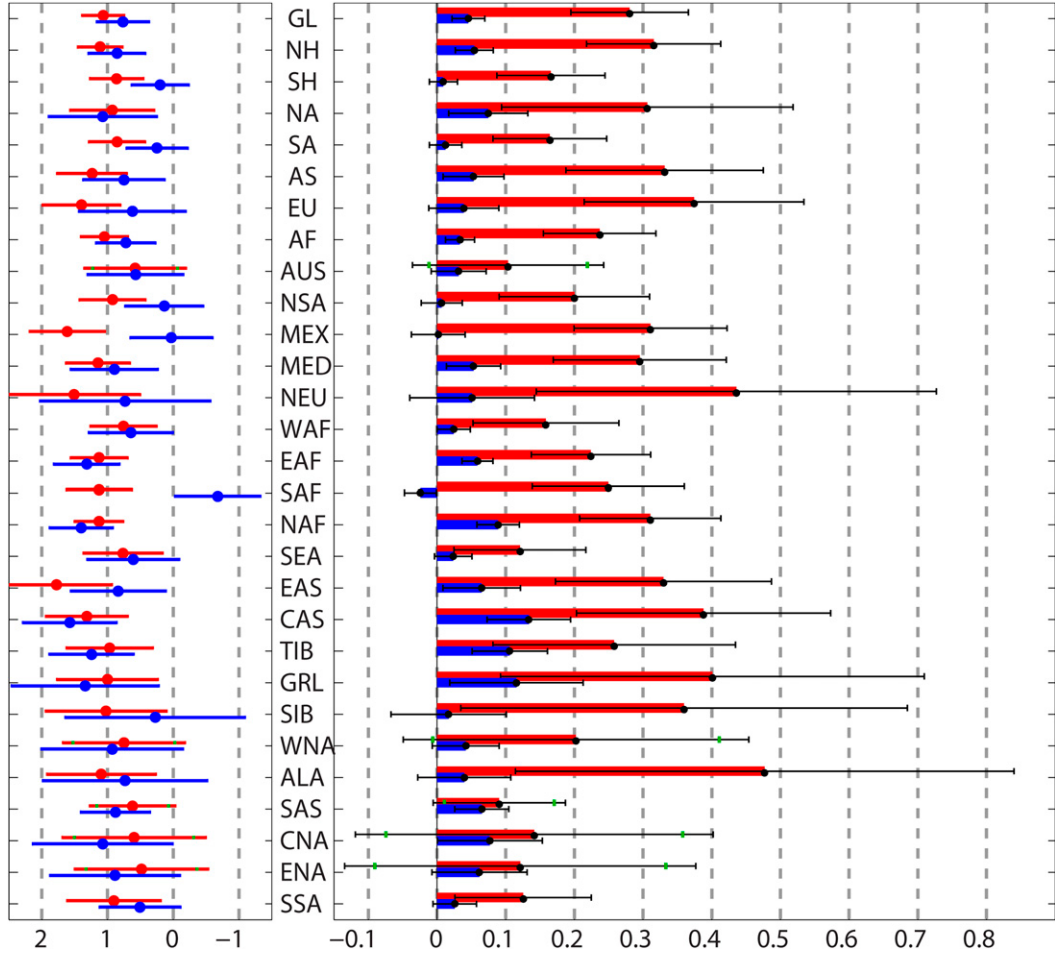


FIG. 8. As in Fig. 7, but for SAT trends over a range of land areas.

boxes where the observed trend is not consistent with the ensemble mean multimodel forced trend ranges from 2% to 6% in these simulations (Fig. 2), grid boxes where the simulated trend from the AMIP runs is not consistent with that in the Historical or HistoricalGHG run are less than 6%, and grid boxes where the simulated trend is not consistent between Historical and HistoricalGHG runs are near 0%. All these fractions are much less than the 95th percentile of the distribution of fractions of grid boxes that give significantly different trends due to internal variability (about 21%). This suggests that observed trends over land are consistent with the ensemble mean multimodel averaged response to either all historical, or greenhouse gas only, or boundary forcings, and that forced trends over land in these three simulations are consistent with each other. Figure 2e indicates that the external natural forcing might have contributed to a small part of land warming due to a positive linear trend in natural forcing over the period of 1979–2005 (Myhre et al. 2013).

Observed and simulated annual mean time series of SAT at various spatial scales are shown in Fig. 5. In general, the observed SAT changes are better reproduced in the AMIP experiment than in coupled experiments in all regions, as expected because prescribed SST in AMIP runs causes interannual variations such as ENSO to occur in the correct years and regions. At the global, hemispheric, and continental scales (except Australia), observed SAT changes are correlated about 0.8–0.9 with the simulated changes in the AMIP, and in the Historical or HistoricalGHG experiments correlations are about 0.6–0.8. In 14 subcontinental regions with significant warming trends at the 5% significance level (except CNA), correlations range from 0.6 to 0.9 in the AMIP, and 0.4 to 0.8 in Historical or HistoricalGHG experiments. Over 14 domains including GL, NH, SA, AF, MED, WAF, EAF, NAF, CAS, TIB, GRL, SEA, and SAS, observed SAT is also correlated with that in HistoricalNAT with correlations above 0.4–0.6. However, at the 5% significance level, the simulated SAT

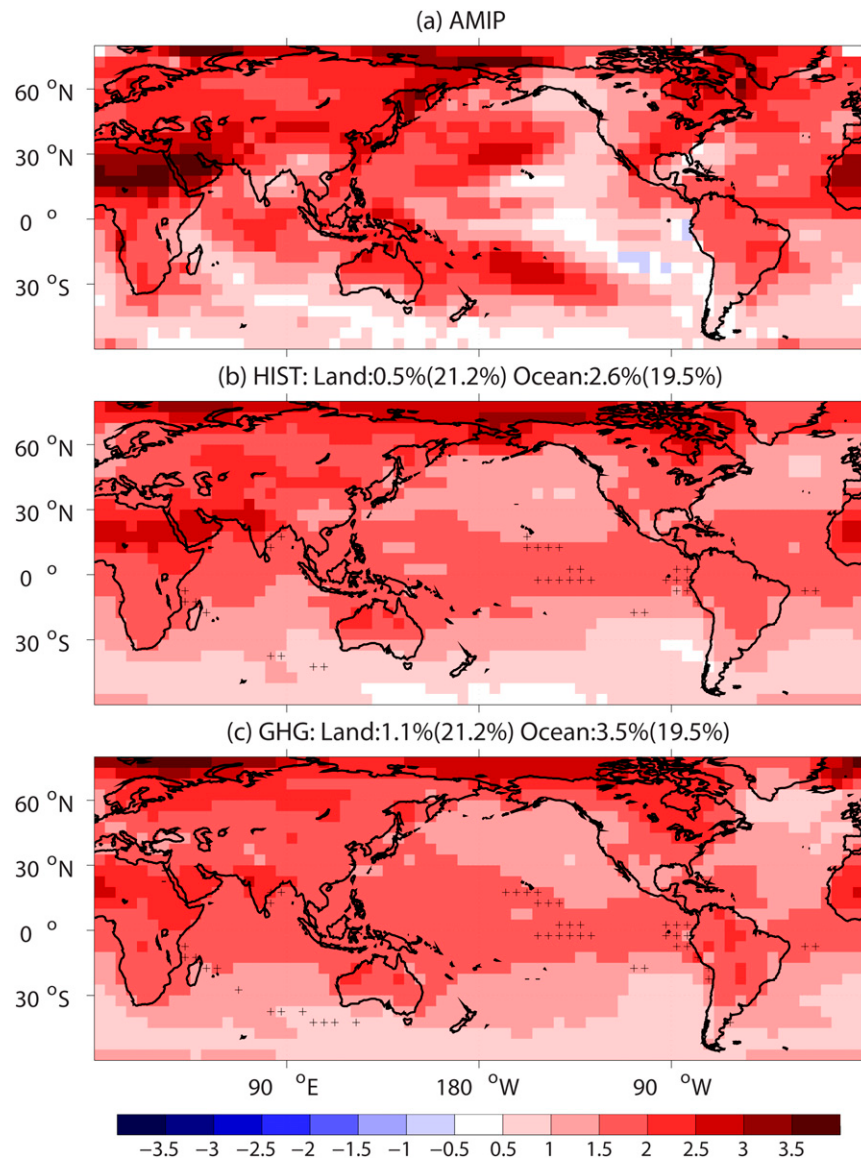


FIG. 9. Simulated trends in annual mean downward longwave radiation ( $\text{W m}^{-2} \text{decade}^{-1}$ ) over 1979–2005 in multimodel averaged (a) AMIP, (b) Historical, and (c) Historical-GHG experiments. Plus (minus) symbols mark individual grid boxes where trends in (b) or (c) are significantly larger (smaller) than that in (a) at the 10% significance level using a two-sided test. Above (b) and (c) are percentages of grid boxes (over land or ocean, respectively) with significantly different trends than in (a), and, in parentheses, the possible range of fractions that could occur due to internal variability.

trend is consistent with the corresponding observed trend on each of the global and hemispheric scales, and in 5 of 6 continental regions and all 20 subcontinental regions in the AMIP, Historical, and HistoricalGHG simulations, but not in the HistoricalNAT simulation (Fig. 6).

At the 5% significance level, an anthropogenic signal is clearly detectable and significantly consistent with

observed SAT changes not only in the global and hemispheric, and 5 of 6 continental scales, but also over 14 of 15 subcontinental regions where observations show significant warming trends at the 5% level (Fig. 8). At the 5% significance level, an anthropogenic signal is also clearly detectable over Alaska and southern South America. Note that the warming trend is statistically significant over Alaska, but insignificant over southern

South America at the 10% level. Figure 8 shows that the NAT signal can be robustly detected over 15 domains, including GL, NH, NA, AS, AF, MED, WAF, EAF, NAF, EAS, CAS, TIB, GRL, SAS, and CAN, at the 5% significance level. Overall, the human-induced GHG increase accounts for most warming observed over 15 of 21 subcontinental regions between 1979 and 2005.

We have shown that both uncoupled (AMIP) and coupled (Historical and HistoricalGHG) simulations are able to capture both the global pattern and magnitudes of the observed trends over land at various spatial scales. In the coupled simulations, the global and tropical oceanic warming pattern is well represented, and nearly all observed ocean and basin-scale warming can be accounted for by prescribed observed historical forcing or greenhouse gas-only forcing. In all three groups of simulations, the warmed ocean moistens and warms the air over land and increases RLDS at the surface through the mechanism of hydrodynamic–radiative teleconnections (Compo and Sardeshmukh 2009). At the 5% significance level, the simulated trends of RLDS, which play a dominant role in surface warming, are consistent across three groups of simulations (Fig. 9). In fact, the fraction of the grid boxes over land and ocean with significantly different trends in surface RLDS between any two groups of AMIP, Historical, and HistoricalGHG runs are less than 1% and 4% respectively, which can be explained by internal climate variations. Fully coupled GCMs forced by prescribed observational radiative forcings are able to successfully capture trend patterns of the global, tropical, and northern midlatitude SST, and thus the global mean as well as most subcontinental aspects of land warming. Therefore, at the global, hemispheric, and 5 of 6 continental scales, and in 15 of 21 subcontinental regions, increasing greenhouse gas concentrations are the ultimate source of land warming at the 5% significance level.

#### 4. Conclusions

Our study establishes the attribution of SST and SAT warming from 1979 to 2005 at a variety of spatial scales and in ocean basins and subcontinental land regions. It is *very likely* (at the 95% confidence level) that the global pattern of SST warming and the warming trend of spatially averaged SST over the world, Northern and Southern Hemispheres, global, hemispheric, the entire tropics and six ocean basins (tropical Indian, western Pacific and Atlantic Oceans, midlatitude North Atlantic, and South and North Pacific) is attributed to anthropogenic forcing. Our attribution results indicate that the

TABLE A1. CMIP3 model runs downloaded for this appendix from [http://www-pcmdi.llnl.gov/ipcc/about\\_ipcc.php](http://www-pcmdi.llnl.gov/ipcc/about_ipcc.php). The top headings identify data types and grids of monthly average surface air temperature (SAT) and net downward longwave radiation (RLDS). Each line lists the number of initial condition ensemble members for historical atmospheric-only runs with prescribed SST and sea ice (AMIP), and historical runs with all anthropogenic and natural forcings (20C3m). All runs cover 1980–99. The bottom row (SUM) shows the number of ensemble members.

Models	SAT		RLDS	
	AMIP	20C3M	AMIP	20C3M
CCM3	16			
CCSM3	1	5	1	5
CNRM-CM3	1	1	1	1
FGOALS1	1	3	1	3
GFDL-CM2	1	3	1	3
GISS1	4	9		9
Had-GEM1		2		2
INMCM3	1	1	1	1
IPSL-CM4	4	2	4	2
MIROC3-LR	1		1	
MIROC3-MR	3	3	3	3
MIROC3-HR		1		1
MPI-ECHAM5	3	4	3	4
MRI-CGCM2	1	4	1	4
NCAR CAM3.5	1			
NCAR-PCML		4		4
SUM	38	42	17	42

global, hemispheric, and basin ocean warming is well reproduced since 1979 in CMIP5 multimodel ensemble mean historical runs including those with all forcing factors or greenhouse gas forcing only. Such correct representation of SST changes is important for representing CMIP5 land warming. The spatial patterns of the CMIP3 and CMIP5 coupled multimodel ensemble mean SAT trends over land were mainly influenced by the pattern of the global SST warming trend over the same period through a hydrodynamic–radiative teleconnection mechanism suggested by Compo and Sardeshmukh (2009) (see the appendix).

With great consistency and agreement across observational datasets and simulations of the climate system with natural and anthropogenic forcings, or boundary forcings, our results suggest that anthropogenic forcing has *very likely* (at the 95% confidence level) contributed to observed SST warming and land warming in 15 subcontinental regions (northern South America, Mexico, Mediterranean, northern Europe, western Africa, eastern Africa, southern Africa, northern Africa, Southeast Asia, East Asia, central Asia, the Tibetan Plateau, Greenland, Siberia, and western North America). Our study is complementary to previous attribution studies that focus on land temperature and SST trends over 50-yr and longer periods (Zhang et al. 2006; Min and Hense

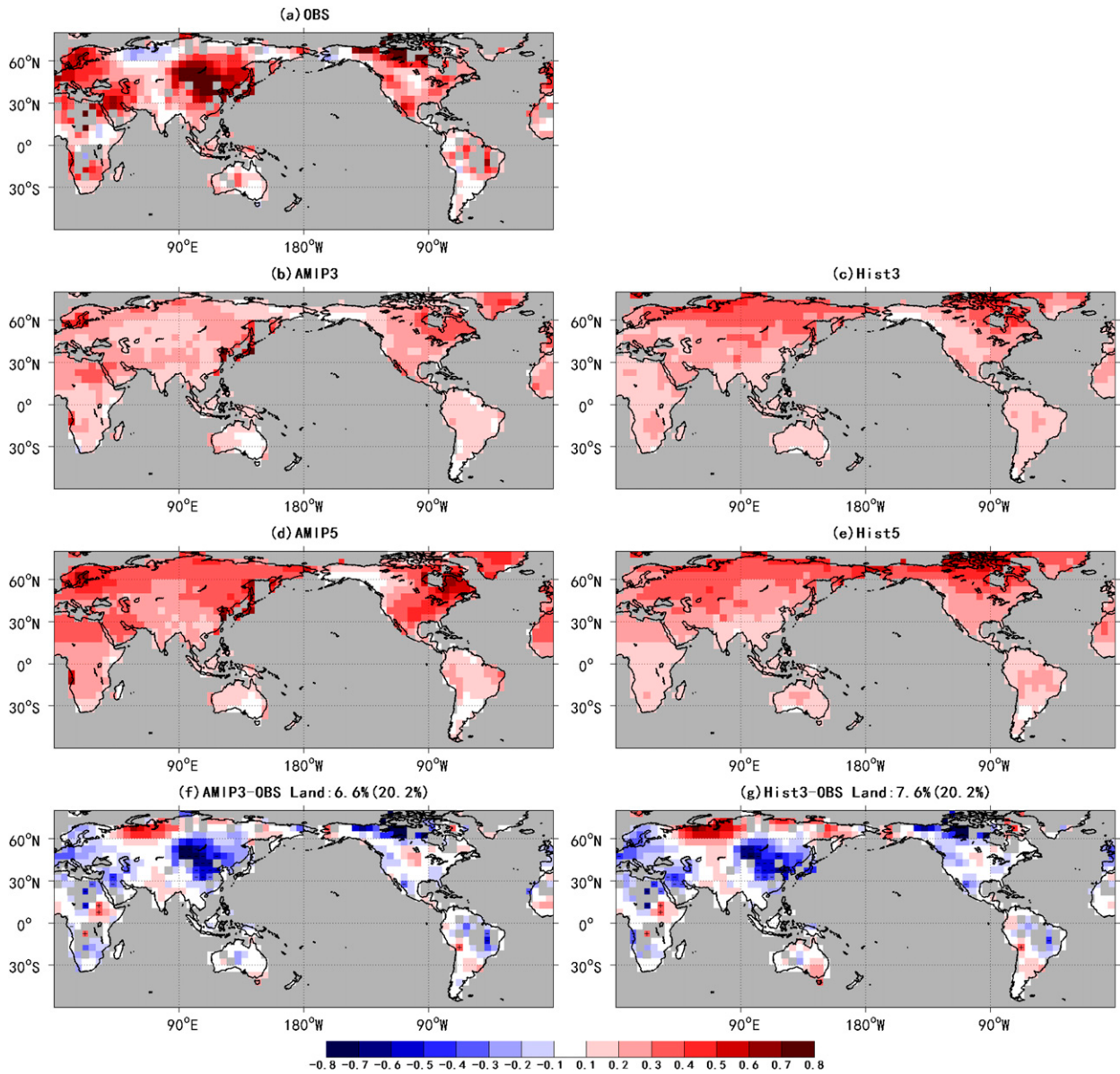


FIG. A1. Trends in annual mean surface temperature ( $^{\circ}\text{C decade}^{-1}$ ) during 1980–99, including observed trends from (a) HadCRUT4, (b) multimodel ensemble-mean trends in four group simulations including CMIP3 AMIP (labeled AMIP3), (c) CMIP3 20C3M (labeled HIST3), (d) CMIP5 AMIP (labeled AMIP5), (e) CMIP5 Historical (labeled HIST5) experiments, (f)–(i) the differences of trends between observations and each simulation, and (j)–(o) differences between pairs of simulations. Plus (minus) symbols mark individual grid boxes with significantly larger (smaller) forced trends than observations in (f)–(i), or mark individual grid boxes with significantly different trends between simulations. At the top of panels (f)–(o) is the fraction of grid boxes (over land or ocean, respectively) with significantly different trends and, in parentheses, the possible range of fractions that could occur due to internal variability.

2006; Jones et al. 2008; Wu 2010; Christidis et al. 2010, 2012; Knutson et al. 2013), and thereby strengthens existing detection and attribution evidence. Previous studies find that grid point trends since 1950 are well represented by the CMIP5 climate models (Bhend and Whetton 2013; Knutson et al. 2013; van Oldenborgh et al.

2013). Our analyses suggest that grid point trends and most subcontinental trends during 1979–2005 are also well represented by the CMIP5 climate models. However, the duration of 1979–2005 is relatively short. Given that numerous CMIP5 analyses have documented models' severe shortfalls, our analysis might be overconfident about

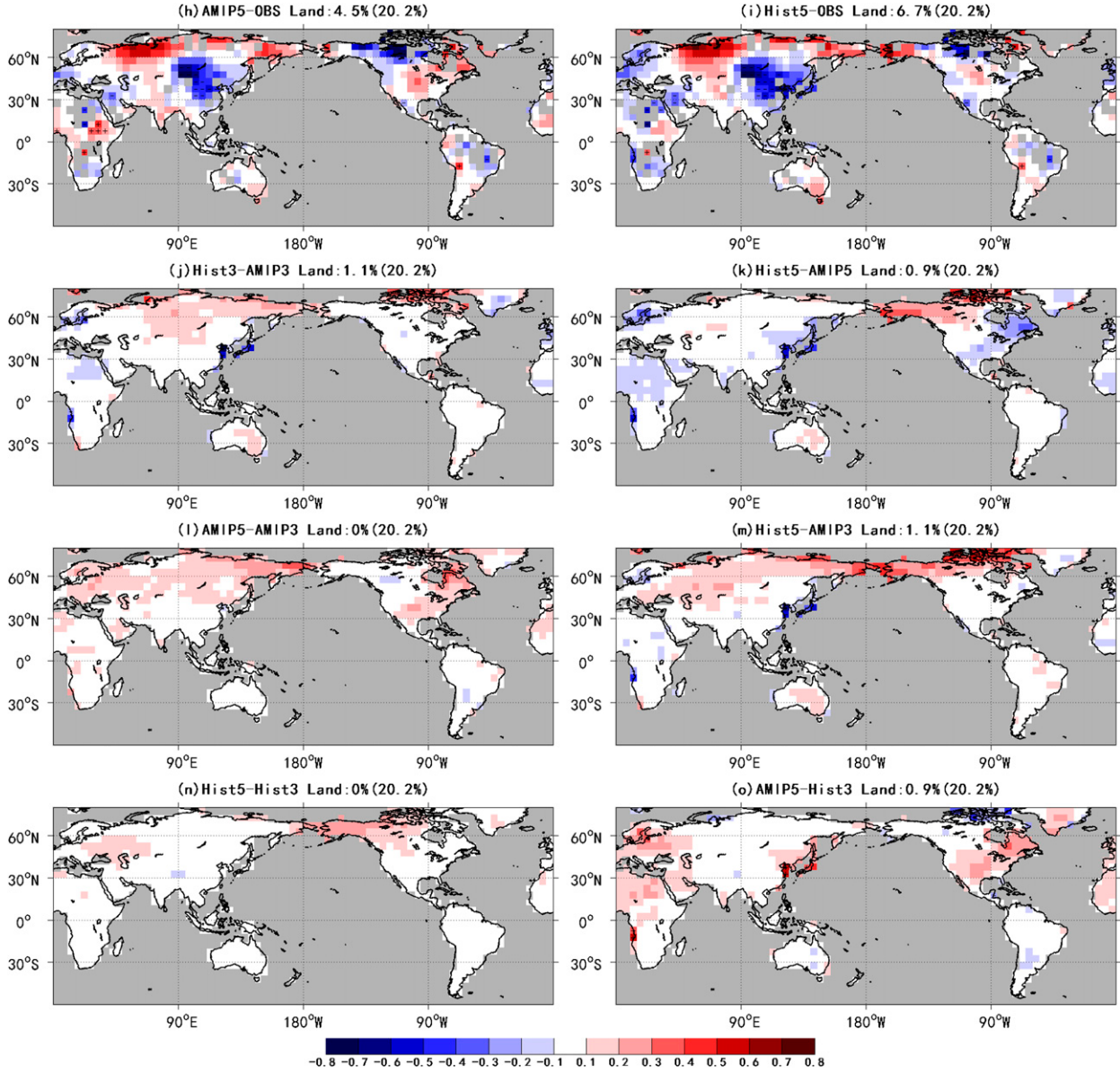


FIG. A1. (Continued)

CMIP5 model skills in simulating observed temperature trends based only on a 27-yr period.

**Acknowledgments.** The authors are grateful for the insightful and constructive comments from three anonymous reviewers. This work is funded by the National Key Scientific Research Plan of China (Grant 2012CB956002) and the National Natural Science Foundation of China (Grant 41075052). This work was also supported by the Jiangsu Collaborative Innovation Center for Climate Change. We also wish to acknowledge the efforts of the many scientists involved in developing, running, and archiving the model simulations that have been used in this

study. Without their efforts, this analysis would not have been possible.

## APPENDIX

### Comparison of Forced Trends from CMIP3 and CMIP5 Experiments during 1980–99

The CMIP5 AMIP-like experiments use forcing including both observed SST and sea ice and atmospheric radiative forcing for 1979–2008 (Taylor et al. 2012), while CMIP3 AMIP experiments use forcing including observed SST and sea ice only (Gates et al. 1999). Here

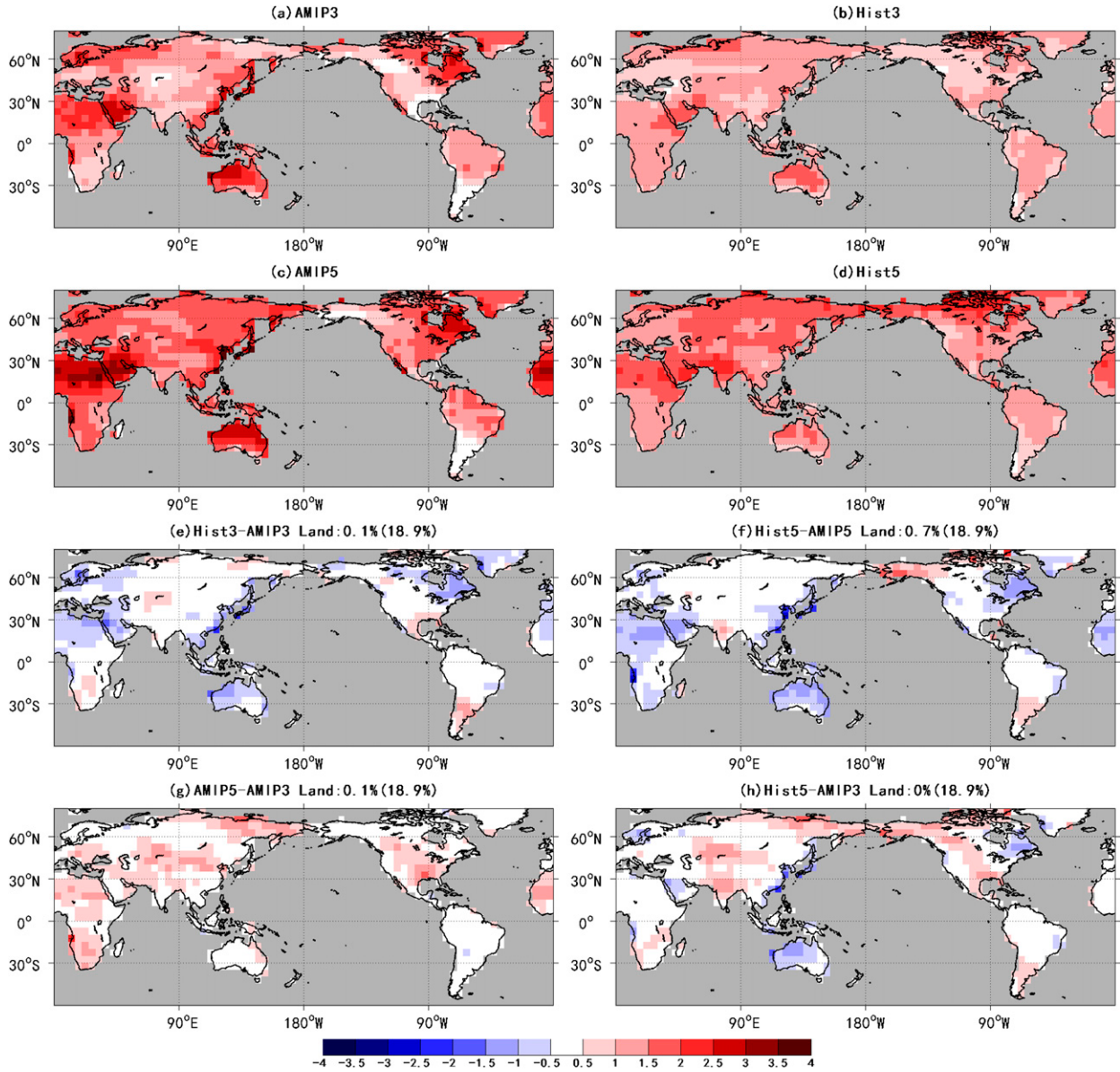


FIG. A2. Multimodel ensemble-mean trends in annual mean downward longwave radiation ( $\text{W m}^{-2} \text{decade}^{-1}$ ) over 1980–99, including (a) CMIP3 AMIP, (b) CMIP3 HIST3, (c) CMIP5 AMIP, (d) CMIP5 Historical simulations, and (e)–(h) differences between pairs of simulations. In (e) to (h), plus (minus) symbols mark individual grid boxes where differences are significantly larger (smaller) at the 10% significance level using a two-sided test. Above those panels are percentages of grid boxes (over land or ocean, respectively) with significantly different trends, and, in parentheses, the possible range of fractions that could occur due to internal variability.

we calculate observed land warming trends in CRUTEM4 and the corresponding forced trends from CMIP3 AMIP and the twentieth century historical simulations (20C3M) experiments of 16 models (Table A1) and from CMIP5 AMIP and Historical experiments (Table 2) over the period of 1980–99. Since the CMIP3 AMIP simulations are run from 1980 to 1999, we focus our comparison on this 20-yr period and use the same methods from

section 2 to analyze model data. Natural variability of linear trends in SAT and RLDS is calculated from the CMIP5 preindustrial control runs.

Figure A1 shows the land warming during 1981–99 for observations and four group simulations, and Fig. A2 displays the increase of RLDS among four group experiments. We find that all four group simulations are able to capture the global pattern and magnitudes of the

observed trends of SAT since the fractions of the grid boxes over land with significantly different trends between observations and each simulation are less than 7.6%, which is much less than the threshold for a significantly different pattern. Difference patterns and magnitudes of land warming between observations and each simulation are similar (Fig. A1f–i), and differences between pairs of simulations are also not significant (Fig. A1j–o). In addition, the four experiment groups simulate consistent trend patterns in downwelling longwave radiation over land (Figs. A2a–d) and the difference patterns (Figs. A2e–h; not all model pairs are shown) are not significant.

The above results demonstrate that the spatial patterns of the CMIP3 or CMIP5 coupled multimodel ensemble mean SAT trends over land were mainly influenced by the pattern of the global SST warming trend over the same period, which is very likely through a hydrodynamic–radiative teleconnection mechanism suggested by Compo and Sardeshmukh (2009). To some degree, results here provide evidence that the indirect land warming response to radiative forcing through the SST response is much larger than the direct land response to radiative forcing in CMIP5 AMIP experiment.

## REFERENCES

- Barnett, T. P., D. W. Pierce, K. AchutaRao, P. Gleckler, B. D. Santer, J. Gregory, and W. Washington, 2005: Penetration of human-induced warming into the world's oceans. *Science*, **309**, 284–287, doi:[10.1126/science.1112418](https://doi.org/10.1126/science.1112418).
- Bhend, J., and P. Whetton, 2013: Consistency of simulated and observed regional changes in temperature, sea level pressure and precipitation. *Climatic Change*, **118**, 799–810, doi:[10.1007/s10584-012-0691-2](https://doi.org/10.1007/s10584-012-0691-2).
- Bindoff, N. L., and Coauthors, 2014: Detection and attribution of climate change: From global to regional. *Climate Change 2013: The Physical Science Basis*, T. F. Stocker, et al., Eds., Cambridge University Press, 867–952.
- Christidis, N., P. A. Stott, F. W. Zwiers, H. Shiogama, and T. Nozawa, 2010: Probabilistic estimates of recent changes in temperature: A multi-scale attribution analysis. *Climate Dyn.*, **34**, 1139–1156, doi:[10.1007/s00382-009-0615-7](https://doi.org/10.1007/s00382-009-0615-7).
- , —, —, —, and —, 2012: The contribution of anthropogenic forcings to regional changes in temperature during the last decade. *Climate Dyn.*, **39**, 1259–1274, doi:[10.1007/s00382-011-1184-0](https://doi.org/10.1007/s00382-011-1184-0).
- Compo, G. P., and P. D. Sardeshmukh, 2009: Oceanic influences on recent continental warming. *Climate Dyn.*, **32**, 333–342, doi:[10.1007/s00382-008-0448-9](https://doi.org/10.1007/s00382-008-0448-9).
- Davis, R. E., 1976: Predictability of sea surface temperature and sea level pressure anomalies over the North Pacific Ocean. *J. Phys. Oceanogr.*, **6**, 249–266, doi:[10.1175/1520-0485\(1976\)006<0249:POSSTA>2.0.CO;2](https://doi.org/10.1175/1520-0485(1976)006<0249:POSSTA>2.0.CO;2).
- Deser, C., and A. S. Phillips, 2009: Atmospheric circulation trends, 1950–2000: The relative roles of sea surface temperature forcing and direct atmospheric radiative forcing. *J. Climate*, **22**, 396–413, doi:[10.1175/2008JCLI2453.1](https://doi.org/10.1175/2008JCLI2453.1).
- Dommenech, D., 2009: The ocean's role in continental climate variability and change. *J. Climate*, **22**, 4939–4952, doi:[10.1175/2009JCLI2778.1](https://doi.org/10.1175/2009JCLI2778.1).
- Enfield, D. B., A. M. Mestas-Nuñez, and P. J. Trimble, 2001: The Atlantic multidecadal oscillation and its relation to rainfall and river flows in the continental U.S. *Geophys. Res. Lett.*, **28**, 2077–2080, doi:[10.1029/2000GL012745](https://doi.org/10.1029/2000GL012745).
- Gates, W. L., and Coauthors, 1999: An overview of the results of the Atmospheric Model Intercomparison Project (AMIP I). *Bull. Amer. Meteor. Soc.*, **80**, 29–55, doi:[10.1175/1520-0477\(1999\)080<0029:AOOTRO>2.0.CO;2](https://doi.org/10.1175/1520-0477(1999)080<0029:AOOTRO>2.0.CO;2).
- Giorgi, F., 2002: Variability and trends of sub-continental scale surface climate in the twentieth century. Part I: Observations. *Climate Dyn.*, **18**, 675–691, doi:[10.1007/s00382-001-0204-x](https://doi.org/10.1007/s00382-001-0204-x).
- Gleckler, P. J., and Coauthors, 2012: Human-induced global ocean warming on multidecadal timescales. *Nat. Climate Change*, **2**, 524–529, xxxx.
- Hegerl, G. C., and Coauthors, 2007: Understanding and attributing climate change. *Climate Change 2007: The Physical Science Basis*, S. Solomon et al., Eds., Cambridge University Press, 663–745.
- Hoerling, M. P., J. W. Hurrell, and T. Xu, 2001: Tropical origins for recent North Atlantic climate change. *Science*, **292**, 90–92, doi:[10.1126/science.1058582](https://doi.org/10.1126/science.1058582).
- Hurrell, J. W., M. P. Hoerling, A. S. Phillips, and T. Xu, 2004: Twentieth century North Atlantic climate change. Part I: Assessing determinism. *Climate Dyn.*, **23**, 371–389, doi:[10.1007/s00382-004-0432-y](https://doi.org/10.1007/s00382-004-0432-y).
- Jones, G. S., P. A. Stott, and N. Christidis, 2008: Human contribution to rapidly increasing frequency of very warm Northern Hemisphere summers. *J. Geophys. Res.*, **113**, D02109, doi:[10.1029/2007JD008914](https://doi.org/10.1029/2007JD008914).
- , —, and —, 2013: Attribution of observed historical near surface temperature variations to anthropogenic and natural causes using CMIP5 simulations. *J. Geophys. Res. Atmos.*, **118**, 4001–4024, doi:[10.1002/jgrd.50239](https://doi.org/10.1002/jgrd.50239).
- Karoly, D. J., and Q. Wu, 2005: Detection of regional surface temperature trends. *J. Climate*, **18**, 4337–4343, doi:[10.1175/JCLI3565.1](https://doi.org/10.1175/JCLI3565.1).
- Kennedy, J. J., N. A. Rayner, R. Q. Smith, M. Saunby, and D. E. Parker, 2011: Reassessing biases and other uncertainties in sea surface temperature observations measured in situ since 1850: 2. Biases and homogenization. *J. Geophys. Res.*, **116**, D14104, doi:[10.1029/2010JD015220](https://doi.org/10.1029/2010JD015220).
- Knutson, T. R., F. Zeng, and A. T. Wittenberg, 2013: Multimodel assessment of regional surface temperature trends. *J. Climate*, **26**, 8709–8743, doi:[10.1175/JCLI-D-12-00567.1](https://doi.org/10.1175/JCLI-D-12-00567.1).
- Livezey, R. E., and W. Y. Chen, 1983: Statistical field significance and its determination by Monte Carlo techniques. *Mon. Wea. Rev.*, **111**, 46–59, doi:[10.1175/1520-0493\(1983\)111<0046:SFSAI>2.0.CO;2](https://doi.org/10.1175/1520-0493(1983)111<0046:SFSAI>2.0.CO;2).
- Mantua, N. J., S. R. Hare, Y. Zhang, J. M. Wallace, and R. C. Francis, 1997: A Pacific interdecadal climate oscillation with impacts on salmon production. *Bull. Amer. Meteor. Soc.*, **78**, 1069–1079, doi:[10.1175/1520-0477\(1997\)078<1069:APICOW>2.0.CO;2](https://doi.org/10.1175/1520-0477(1997)078<1069:APICOW>2.0.CO;2).
- Mardia, K. V., J. T. Kent, and J. M. Bibby, 1979: *Multivariate Analysis*. Academic Press, 521 pp.
- Min, S., and A. Hense, 2006: A Bayesian assessment of climate change using multimodel ensembles. Part I: Global mean surface temperature. *J. Climate*, **19**, 3237–3256, doi:[10.1175/JCLI3784.1](https://doi.org/10.1175/JCLI3784.1).

- Myhre, G., and Coauthors, 2013: Anthropogenic and natural radiative forcing. *Climate Change 2013: The Physical Science Basis*, T. F. Stocker, et al., Eds., Cambridge University Press, 659–740.
- Pegion, P. J., and A. Kumar, 2010: Multimodel estimates of atmospheric response to modes of SST variability and implications for droughts. *J. Climate*, **23**, 4327–4341, doi:[10.1175/2010JCLI3295.1](https://doi.org/10.1175/2010JCLI3295.1).
- Pierce, D. W., P. J. Gleckler, T. P. Barnett, B. D. Santer, and P. J. Durack, 2012: The fingerprint of human-induced changes in the ocean's salinity and temperature fields. *Geophys. Res. Lett.*, **39**, L21704, doi:[10.1029/2012GL053389](https://doi.org/10.1029/2012GL053389).
- Power, S., T. Casey, C. Folland, A. Colman, and V. Mehta, 1999: Inter-decadal modulation of the impact of ENSO on Australia. *Climate Dyn.*, **15**, 319–324, doi:[10.1007/s003820050284](https://doi.org/10.1007/s003820050284).
- Rosenzweig, C., and Coauthors, 2008: Attributing physical and biological impacts to anthropogenic climate change. *Nature*, **453**, 353–358, doi:[10.1038/nature06937](https://doi.org/10.1038/nature06937).
- Schneider, E. K., L. Bengtsson, and Z. Hu, 2003: Forcing of Northern Hemisphere climate trends. *J. Atmos. Sci.*, **60**, 1504–1521, doi:[10.1175/1520-0469\(2003\)060<1504:FONHCT>2.0.CO;2](https://doi.org/10.1175/1520-0469(2003)060<1504:FONHCT>2.0.CO;2).
- Shin, S.-I., and P. D. Sardeshmukh, 2011: Critical influence of the pattern of tropical ocean warming on remote climate trends. *Climate Dyn.*, **36**, 1577–1591, doi:[10.1007/s00382-009-0732-3](https://doi.org/10.1007/s00382-009-0732-3).
- Taylor, K. E., R. J. Stouffer, and G. A. Meehl, 2012: An overview of CMIP5 and the experiment design. *Bull. Amer. Meteor. Soc.*, **93**, 485–498, doi:[10.1175/BAMS-D-11-00094.1](https://doi.org/10.1175/BAMS-D-11-00094.1).
- Trenberth, K. E., and Coauthors, 2007: Observations: Surface and atmospheric climate change. *Climate Change 2007: The Physical Science Basis*, S. Solomon et al., Eds., Cambridge University Press, 235–336.
- van Oldenborgh, G. J., F. J. Doblas Reyes, S. S. Drijfhout, and E. Hawkins, 2013: Reliability of regional climate model trends. *Environ. Res. Lett.*, **8**, 014055, doi:[10.1088/1748-9326/8/1/014055](https://doi.org/10.1088/1748-9326/8/1/014055).
- Wu, Q., 2010: Associations of diurnal temperature range change with the leading climate variability modes during the Northern Hemisphere wintertime and their implication on the detection of regional climate trends. *J. Geophys. Res.*, **115**, D19101, doi:[10.1029/2010JD014026](https://doi.org/10.1029/2010JD014026).
- , and D. J. Karoly, 2007: Implications of changes in the atmospheric circulation on the detection of regional surface air temperature trends. *Geophys. Res. Lett.*, **34**, L08703, doi:[10.1029/2006GL028502](https://doi.org/10.1029/2006GL028502).
- Zhang, X., F. W. Zwiers, and P. A. Stott, 2006: Multi-model multi-signal climate change detection at regional scale. *J. Climate*, **19**, 4294–4307, doi:[10.1175/JCLI3851.1](https://doi.org/10.1175/JCLI3851.1).